Available online at www.sciencedirect.com

ScienceDirect

IFAC Papers Online CONFERENCE PAPER ARCHIVE

IFAC PapersOnLine 59-22 (2025) 525–530

# High-Fidelity Process Plant Modeling of an Unmanned Sailboat with a Wing Sail Based on Multi-body Dynamics

**Bo Peng** * **Yang An** * **Mengwei Zhang** * **Zhengru Ren** *,**

* *Institute for Ocean Engineering, Shenzhen International Graduate School, Tsinghua University, Shenzhen 518055, China (email: pb23@mails.tsinghua.edu.cn, {anyang, zhangmengw, zhengru.ren}@sz.tsinghua.edu.cn)*

** *School of Ocean and Civil Engineering, Shanghai Jiao Tong University, Shanghai 200240, China (email: zhengru.ren@sz.tsinghua.edu.cn)*

**Abstract:** This paper presents , to the best of our knowledge, the first MATLAB/Simulink high-fidelity process plant model for an unmanned sailboat equipped with a wing sail, integrating multi-body dynamics with comprehensive aerodynamics and hydrodynamics modeling. The six degrees of freedom (6-DoF) nonlinear model incorporates frequency-domain hydrodynamic coefficients computed via WAMIT. The aerodynamic and hydrodynamic loads on the sail, rudder, and keel are uniformly modeled using the Morison equation, where local lift and drag forces are calculated based on precomputed CFD-derived coefficient maps. Distributed fluid loads acting on the foils are resolved through the discretized panel-based method. Implemented in MATLAB/Simulink using modular subsystems, the framework supports bidirectional coupling between rigid body dynamics and environmental forces. The model's physical consistency is validated through a series of static force tests, as well as through dynamic response analysis under wave-induced excitations.



*Keywords:* Unmanned sailboat, process plant model, multi-body dynamics, hydrodynamics, aerodynamics.

## 1. INTRODUCTION

Unmanned sailboats are receiving increasing attention in recent years due to their potential for long-endurance, energy-autonomous marine operations (Tipsuwan et al., 2023). These wind-powered vessels offer significant advantages over conventional propulsion systems, particularly for missions such as oceanographic monitoring, environmental sensing, and maritime surveillance (An et al., 2021). By harnessing renewable wind energy, they achieve extended endurance without the need for large fuel reserves or frequent servicing, making them attractive for persistent deployment in remote ocean regions (Plumet et al., 2014; Sun et al., 2020).

Despite these advantages, the dynamics of unmanned sailboats are inherently complex due to the nonlinear and coupled interactions between multiple subsystems, including the sail, rudder, keel, and hull, as well as the influence of highly variable environmental conditions such as wind, waves, and currents (Gu et al., 2022; Zhang et al., 2021). These interactions present substantial challenges for modeling and control, particularly in the presence of unsteady aerodynamics, wave-induced motions, and stochastic disturbances (Peng et al., 2023, 2022, 2021; Zhang and Ren, 2025).

To enable effective autonomous operation, accurate dynamic modeling of unmanned sailboats is essential. Two modeling paradigms are commonly adopted in this context, i.e., the control plant model and the process plant model (Fossen, 2011; Qin et al., 2023; Wang et al., 2023). The control plant model is primarily developed for real-time control tasks such as stabilization, guidance, and trajectory tracking (Deng et al., 2019; Peng et al., 2025; Xiao and Jouffroy, 2013). These models are typically simplified to reduce computational burden, often by linearizing or approximating the aerodynamic and hydrodynamic forces. While such simplifications facilitate onboard implementation, they often neglect critical transient behaviors including flow separation, hull oscillations, and cross-coupling effects.

In contrast, the process plant model aims to capture the full physical chain from environmental excitations to system response (Ma et al., 2025). This type of model incorporates detailed aerodynamics and hydrodynamics modeling, nonlinear multi-body dynamics, and time-varying external loads, thereby providing a high-fidelity representation of sailboat motion. Process plant models are particularly valuable for system design, controller validation, failure

⋆ This work was supported by the Natural Science Foundation of Guangdong Province, China (Grant No.2024A1515011731), the Shenzhen Science and Technology Program (Grant No.WDZC20231128135104001).

**Corresponding author: Zhengru Ren.

2405-8963 
Peer review under responsibility of International Federation of Automatic Control.
10.1016/j.ifacol.2025.11.687

scenario testing, and digital twin development (Chen et al., 2025; Shah et al., 2021). However, their application to unmanned sailboats remains relatively underexplored compared to other maritime domains such as offshore platforms and ship motion prediction (Ren et al., 2018).

Existing research has largely focused on control plant models (Qin et al., 2024; Viel et al., 2019), which offer practical advantages in terms of computational efficiency and onboard implementation. However, these models often rely on simplified force representations, assume decoupled subsystem dynamics, and neglect wave-induced hull motions and environment-driven transients. Current performance evaluations and control strategies are typically validated using simplified models that neglect key physical interactions. Although effective for low-level control objectives, their limited physical fidelity reduces their applicability in high-precision simulation, design validation, or performance evaluation under extreme sea states.

To address this modeling gap, this paper presents a high-fidelity process plant model for unmanned sailboats. The model captures the six degrees of freedom (6-DoF) dynamics of the sail, rudder, keel, and hull within a multi-body dynamics framework that accounts for both internal coupling and environmental excitations, including turbulent wind and irregular waves.

Hydrodynamic responses of the hull under wave excitation are obtained using frequency-domain potential-flow analysis via WAMIT. Forces acting on the foils (wing sail, rudder, and keel) are computed using a Morison equation-based formulation. The lift and drag coefficients are precomputed from CFD data of representative airfoils, ensuring nonlinear aerodynamic and hydrodynamic characteristics are accurately captured. Distributed fluid loads on the foils are resolved through the discretized panel-based method. The main contributions of this study are as follows:

(1) A unified 6-DoF multi-body dynamics model capturing coupled sail-rudder-keel-hull interactions under numerically simulated wind and wave conditions.
(2) Physically consistent force modeling via integration of WAMIT-derived wave-induced hydrodynamics and precomputed CFD-based lift/drag coefficients for the foils.
(3) A modular and computationally efficient simulation framework designed for real-time execution and extensibility for advanced control applications.

This paper is organized as follows: Section 2 establishes the reference frames and the modeling assumptions; Section 3 characterizes the wind, wave and current loads; Section 4 develops the 6-DoF multi-body dynamics framework integrating the sail, rudder, and hull interactions; Section 5 systematically validates model fidelity through static force characterization and dynamic response analysis under wave-induced excitations; Section 6 summarizes the paper and suggests future research directions.

## 2. PRELIMINARIES

The notations used throughout this paper are tabulated in Table 1.

Table 1. Notation and definitions

| Notation | Definition |
|---|---|
| $\mathbb{R}$ | Field of real numbers |
| $\mathbb{R}^{n\times m}$ | Space of $n \times m$ real matrices |
| $\mathbf{0}_{n\times m}$ | Zero matrix of size $n \times m$ |
| $\{n\},\{b\},\{s\},\{r\},\{k\}$ | NED, body-fixed, sail, rudder, and keel reference frames |
| $\boldsymbol{a}^j$ | Vector $\boldsymbol{a}$ expressed in frame $\{j\}$ |
| c·, s·, t· | $\cos(\cdot)$, $\sin(\cdot)$, $\tan(\cdot)$ |
| $\boldsymbol{\eta} \in \mathbb{R}^6$ | Pose vector [position; Euler angles] |
| $\boldsymbol{p} \in \mathbb{R}^3$ | Position vector |
| $\boldsymbol{\Theta}_{ab} \in \mathbb{R}^3$ | Euler angles from $\{a\}$ to $\{b\}$ |
| $\boldsymbol{v}_{tw}, \boldsymbol{v}_{aw} \in \mathbb{R}^3$ | True/Apparent wind velocity |
| $\boldsymbol{v}_{tc}, \boldsymbol{v}_{ac} \in \mathbb{R}^3$ | True/Apparent current velocity |
| $\alpha_{tw}, \alpha_{aw}$ | True/apparent wind angles |
| $\alpha_{tc}, \alpha_{ac}$ | True/apparent current angles |
| $L, D \in \mathbb{R}$ | Lift and drag forces |
| $C_L(\alpha), C_D(\alpha) : \mathbb{R} \mapsto \mathbb{R}$ | Lift and drag coefficients as functions of attack angle |
| $\alpha \in \mathbb{R}$ | Angle of attack |
| $\rho \in \mathbb{R}$ | Air/water density |
| $N \in \mathbb{R}$ | Number of discretized panels on the foil |
| $A \in \mathbb{R}$ | Area of the foil |
| $\bar{v}_w, v_w, v_{10}, \bar{v}_c, v_c \in \mathbb{R}$ | Mean wind, true wind, 10m wind, mean current, current speeds |
| $z_w \in \mathbb{R}$ | Wind reference height |
| $\epsilon \in \mathbb{R}$ | Wind shear exponent |
| $T \in \mathbb{R}$ | Turbulence time scale |
| $\sigma_w \in \mathbb{R}$ | Standard deviation of the wind fluctuation |
| $\xi(t) \in \mathbb{R}$ | White noise with unit spectral density |
| $TI \in \mathbb{R}$ | Turbulence intensity |
| $S(\omega) : \mathbb{R} \mapsto \mathbb{R}$ | Wave spectral density function |
| $H_s \in \mathbb{R}$ | Significant wave height |
| $T_p, T_0, T_z \in \mathbb{R}$ | Peak/Mean/Zero-crossing periods |
| $\gamma \in \mathbb{R}$ | JONSWAP peak enhancement factor |
| $\sigma \in \mathbb{R}$ | Spectral width parameter |
| $\omega \in \mathbb{R}$ | Wave angular frequency |
| $\boldsymbol{\nu} \in \mathbb{R}^6$ | Vessel velocity [linear; angular] |
| $\boldsymbol{v}, \boldsymbol{\omega} \in \mathbb{R}^3$ | Linear/Angular velocity |
| $\boldsymbol{\nu}_c \in \mathbb{R}^6$ | Current velocity [linear; angular] |
| $\boldsymbol{\nu}_r \in \mathbb{R}^6$ | Relative flow velocity |
| $\boldsymbol{R}_a^b \in \mathbb{R}^{3\times3}$ | Rotation matrix from $\{a\}$ to $\{b\}$ |
| $\boldsymbol{T}(\boldsymbol{\Theta}) \in \mathbb{R}^{3\times3}$ | Euler angle transformation matrix |
| $\boldsymbol{r}_s, \boldsymbol{r}_r \in \mathbb{R}^3$ | Center of effect (CoE) position of sail/rudder |
| $\boldsymbol{d}_{ab} \in \mathbb{R}^3$ | Reference frame translation offset vector from $\{a\}$ to $\{b\}$ |
| $\boldsymbol{M}_{\mathrm{RB}} \in \mathbb{R}^{6\times6}$ | Rigid-body mass matrix |
| $\boldsymbol{M}_{\mathrm{A}} \in \mathbb{R}^{6\times6}$ | Added mass matrix |
| $\boldsymbol{C}_{\mathrm{RB}}(\boldsymbol{\nu}_r) \in \mathbb{R}^{6\times6}$ | Rigid-body Coriolis matrix |
| $\boldsymbol{C}_{\mathrm{A}}(\boldsymbol{\nu}_r) \in \mathbb{R}^{6\times6}$ | Added-mass Coriolis matrix |
| $\boldsymbol{D} \in \mathbb{R}^{6\times6}$ | Linear damping matrix |
| $\boldsymbol{D}_n(\boldsymbol{\nu}_r) \in \mathbb{R}^{6\times6}$ | Nonlinear damping matrix |
| $\boldsymbol{g}(\boldsymbol{\eta}) \in \mathbb{R}^6$ | Restoring force vector |
| $\boldsymbol{\tau}, \boldsymbol{\tau}_s, \boldsymbol{\tau}_r, \boldsymbol{\tau}_k \in \mathbb{R}^6$ | Control input/Sail/Rudder/Keel force/moment vectors |
| $\boldsymbol{\tau}_{\mathrm{wave}}, \boldsymbol{\tau}_{\mathrm{wave1}}, \boldsymbol{\tau}_{\mathrm{wave2}} \in \mathbb{R}^6$ | Total/1st/2nd-order wave forces |
| $\delta_s, \delta_r \in \mathbb{R}$ | Sail and rudder angles |

### *2.1 Reference frames*

In order to clearly describe the relative motion and interactions between the hull, sail, rudder, and the external environment, as shown in Fig. 1, the following four reference frames are needed:

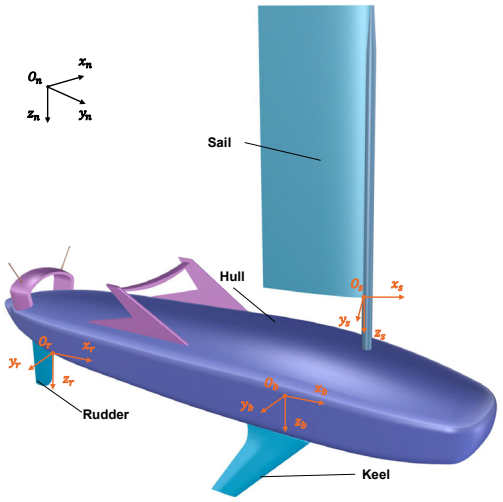


Fig. 1. Reference frames definition of the unmanned sailboat.

- The North-East-Down (NED) reference frame $\{n\} = (x_n, y_n, z_n)$, with its origin $O_n$, is defined relative to the Earth's reference ellipsoid.
- The body-fixed reference frame $\{b\} = (x_b, y_b, z_b)$ is a moving reference frame fixed to the hull, with its origin $O_b$ located at the center of gravity of the sailboat.
- The sail reference frame $\{s\} = (x_s, y_s, z_s)$ is defined with its origin $O_s$ located at the base of the mast, where the sail meets the hull.
- The rudder reference frame $\{r\} = (x_r, y_r, z_r)$ is defined with its origin $O_r$ at the intersection of the rudder's leading edge and the hull.

### 2.2 Modeling framework

The proposed modeling framework integrates high-fidelity tools to enable comprehensive characterization of vessel dynamics. Multisurf is employed to generate precise hull geometries, while WAMIT is used to compute potential-flow hydrodynamic coefficients, including wave-induced loads, added mass, and radiation damping. The aerodynamic and hydrodynamic loads on the sail, rudder, and keel are uniformly modeled using the Morison equation, where local lift and drag forces are calculated based on precomputed CFD-derived coefficient maps. Distributed fluid loads are resolved through the discretized panel-based method. An overview of the modeling framework is illustrated in Fig. 2.

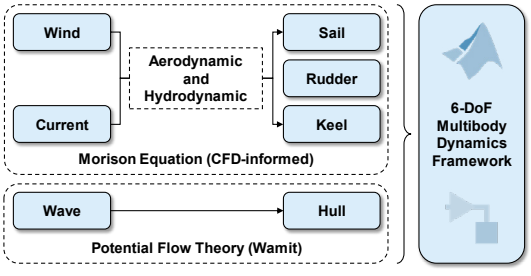


Fig. 2. Overview of the modeling framework.

The model is implemented in the Matlab/Simulink, providing a modular and extensible platform suitable for dynamic simulations and control system design. The foundation for the subsequent modeling is based on the following key assumptions i.e.,

(1) The sail, rudder, keel, and hull are assumed as rigid bodies, with rigid connections between the hull and other components.
(2) The fluid dynamics of both the sail and rudder are characterized using standard foil lift and drag coefficients.
(3) The force of the wind acting on the hull is considered negligible.
(4) The ocean currents are assumed to be constant and irrotational in the frame $\{n\}$.

## 3. ENVIRONMENTAL MODELING

### 3.1 Wind field and current

In the near-surface layer, wind speed varies with height due to surface roughness and atmospheric stability. This variation is characterized by the wind shear coefficient $\epsilon$, which describes the rate at which wind speed increases with altitude in the vertical plane perpendicular to the wind direction. The wind speed at height $z_w$ is expressed as

$$v_w(z_w) = v_{10}\left(\frac{z_w}{10}\right)^{\epsilon}, \tag{1}$$

where the typical values of $\epsilon$ depend on the surface roughness and atmospheric conditions.

Turbulence in the wind field is modeled as a first-order Gauss–Markov process, capturing the stochastic nature of atmospheric fluctuations. The true wind velocity vector in the inertial frame $\{n\}$ is expressed as $\boldsymbol{v}_{tw}^n = [v_w\cos(\alpha_{tw}), v_w\sin(\alpha_{tw}), 0]^\top$, where the wind speed $v_w$ is composed of a mean component $\bar{v}_w$ and a fluctuating component $\delta v$ due to turbulence i.e., $v_w(t) = \bar{v}_w + \delta v(t)$.

The turbulence-induced fluctuation $\delta v(t)$ is modeled as a zero-mean, stationary Gaussian–Markov process governed by the stochastic differential equation $\dot{\delta v}(t) = -1/T\delta v(t) + \sigma_w\xi(t)$, where $\sigma_w = TI\cdot\bar{v}_w$. Similarly, the true current velocity vector is given by $\boldsymbol{v}_{tc}^n = [v_c\cos(\alpha_{tc}), v_c\sin(\alpha_{tc}), 0]^\top$.

### 3.2 Wave modeling

To model the irregular sea states, the spectrum of Joint North Sea Wave Project (JONSWAP) is adopted. The spectral density function is given by

$$S(\omega) = 155\frac{H_s^2}{T_1^4}\omega^{-5}\exp\left(-\frac{944}{T_1^4}\omega^{-4}\right)\gamma^Y, \tag{2}$$

where the exponential term $Y$ modifies the spectrum around the peak frequency and is expressed as $Y = \exp[-\left((0.191\omega T_1 - 1)/\sqrt{2}\sigma\right)^2]$, where

$$\sigma = \begin{cases} 0.07, & \text{for } \omega \le 5.24/T_1, \\ 0.09, & \text{for } \omega > 5.24/T_1, \end{cases}$$

with $T_1 = 0.834T_0 = 1.073T_z$. In addition, the directionality of wave is included in the simulation through a prescribed heading angle.

## 4. DYNAMIC MODELING

### 4.1 Kinematics and kinetics

Table 2. Degrees of freedom with corresponding variables

| DoF | Description | $\boldsymbol{\nu}$ | $\boldsymbol{\eta}$ |
|---|---|---|---|
| 1 | surge | $u$ | $x$ |
| 2 | sway | $v$ | $y$ |
| 3 | heave | $w$ | $z$ |
| 4 | roll | $p$ | $\phi$ |
| 5 | pitch | $q$ | $\theta$ |
| 6 | yaw | $r$ | $\psi$ |

As standard in marine vehicle dynamics, the 6-DoF motion of sailboats (defined in Table 2) is governed by the following coupled kinematic and kinetic equations (Fossen, 2011; Xiao and Jouffroy, 2013)

$$\dot{\boldsymbol{\eta}} = \boldsymbol{J}(\boldsymbol{\eta})\,\boldsymbol{\nu}, \tag{3a}$$

$$\boldsymbol{M}\dot{\boldsymbol{\nu}} + \boldsymbol{C}(\boldsymbol{\nu}_r)\,\boldsymbol{\nu}_r + \boldsymbol{D}(\boldsymbol{\nu}_r)\,\boldsymbol{\nu}_r + \boldsymbol{g}(\boldsymbol{\eta}) = \boldsymbol{\tau} + \boldsymbol{\tau}_{\text{wave}} + \boldsymbol{\tau}_k, \tag{3b}$$

where $\boldsymbol{\nu}_r = \boldsymbol{\nu} - \boldsymbol{\nu}_c$, $\boldsymbol{\tau} = \boldsymbol{\tau}_s + \boldsymbol{\tau}_r$, and

$$\boldsymbol{J}(\boldsymbol{\eta}) = \begin{bmatrix} \boldsymbol{R}_b^n(\boldsymbol{\Theta}_{bn}) & \boldsymbol{0}_{3\times3} \\ \boldsymbol{0}_{3\times3} & \boldsymbol{T}(\boldsymbol{\Theta}_{bn}) \end{bmatrix},$$

with

$$\boldsymbol{R}_b^n(\boldsymbol{\Theta}_{bn}) = \begin{bmatrix} c\psi c\theta & s\phi s\theta c\psi - s\psi c\phi & s\phi s\psi + s\theta c\phi c\psi \\ s\psi c\theta & s\phi s\psi s\theta + c\phi c\psi & -s\phi c\psi + s\psi s\theta c\phi \\ -s\theta & s\phi c\theta & c\phi c\theta \end{bmatrix},$$

$$\boldsymbol{T}(\boldsymbol{\Theta}_{bn}) = \begin{bmatrix} 1 & s\phi t\theta & c\phi t\theta \\ 0 & c\phi & -s\phi \\ 0 & s\phi/c\theta & c\phi/c\theta \end{bmatrix}.$$

The hydrodynamic coefficient matrices of the sailboat kinetics (3b) is given by $\boldsymbol{M} = \boldsymbol{M}_{\text{RB}} + \boldsymbol{M}_{\text{A}}$, $\boldsymbol{C}(\boldsymbol{\nu}_r) = \boldsymbol{C}_{\text{RB}}(\boldsymbol{\nu}_r) + \boldsymbol{C}_{\text{A}}(\boldsymbol{\nu}_r)$, and $\boldsymbol{D}(\boldsymbol{\nu}_r) = \boldsymbol{D} + \boldsymbol{D}_n(\boldsymbol{\nu}_r)$, where these matrices are further defined in Fossen (2011). In this study, they are obtained through numerical simulation in WAMIT, with frequency-domain potential flow theory applied to the hull geometry shown in Fig.1.

### 4.2 Forces and moments generated by the sail, rudder, and keel

The aerodynamic and hydrodynamic loads acting on the sail and rudder are computed using the discretized panel-based method. Each foil is divided into a finite number of panels, where the local apparent flow velocity and angle of attack are determined via reference frame transformations. At each panel, lift and drag forces are calculated based on a Morison equation, with pre-tabulated lift and drag coefficients from the standard airfoil. The total force and moment acting on each foil are obtained by summing the contributions of all panels in the $\{b\}$ frame.

For a general foil $\iota \in \{s, r, k\}$, representing the sail, rudder, or keel, the apparent flow velocity at the $i$-th panel in the local reference frame $\{\iota\}$ is given by

$$\boldsymbol{v}_{a,i}^{\iota} = \boldsymbol{R}_b^{\iota}\boldsymbol{v}_{a,i}^{b}, \tag{5}$$

where $\boldsymbol{v}_{a,i}^{b} = \boldsymbol{v}_t^b - \boldsymbol{v}^b - \boldsymbol{\omega}^b \times \boldsymbol{r}_{\iota,i}^b$, $\boldsymbol{v}_t^b = \boldsymbol{R}_n^b\boldsymbol{v}_t^n$, $\boldsymbol{r}_{\iota,i}^{\iota} = [x_{\iota,i}, y_{\iota,i}, z_{\iota,i}]^\top$, $\boldsymbol{r}_{\iota,i}^b = \boldsymbol{R}_b^{\iota\top}\boldsymbol{r}_{\iota,i}^{\iota} + \boldsymbol{d}_{\iota b,i}$, and $\boldsymbol{v}_{a,i}^{\iota} = [v_{au,i}, v_{av,i}, v_{aw,i}]^\top$. The angle of attack and apparent flow speed are computed as $\alpha_{\iota,i} = \arctan 2(v_{av,i}, -v_{au,i})$ and $v_{a,i} = \sqrt{v_{au,i}^2 + v_{av,i}^2}$.

The lift and drag forces on the $i$-th panel are computed using a Morison equation-based formulation i.e.,

$$L_{\iota,i} = \frac{1}{2}\rho_\iota A_{\iota,i} v_{a,i}^2 C_L(\alpha_{\iota,i}), \tag{6a}$$

$$D_{\iota,i} = \frac{1}{2}\rho_\iota A_{\iota,i} v_{a,i}^2 C_D(\alpha_{\iota,i}), \tag{6b}$$

where $\rho_\iota$ denotes the fluid density (air for sail, water for rudder and keel). The local force vector in the frame $\{\iota\}$ is then $\boldsymbol{F}_{\iota,i}^{\iota} = [-D_{\iota,i}, L_{\iota,i}, 0]^\top$. Transforming to the frame $\{b\}$, the total force and moment exerted by the foil $\iota$ are obtained as $\boldsymbol{F}_{\iota}^{b} = \sum_{i=1}^{N_\iota} \boldsymbol{R}_{\iota}^{b}\boldsymbol{F}_{\iota,i}^{\iota}$, $\boldsymbol{M}_{\iota}^{b} = \sum_{i=1}^{N_\iota} \boldsymbol{r}_{\iota,i}^{b} \times \boldsymbol{R}_{\iota}^{b}\boldsymbol{F}_{\iota,i}^{\iota}$, and the resulting generalized force vector is $\boldsymbol{\tau}_{\iota}^{b} = [\boldsymbol{F}_{\iota}^{b}, \boldsymbol{M}_{\iota}^{b}]^\top$.

The keel is modeled following the same discretized panel-based method as the rudder. However, the keel is rigidly mounted beneath the hull, its orientation remains fixed and is treated as an external input rather than a controllable variable in the control system.

### 4.3 Wave-induced forces and moments

The wave-induced forces and moments are critical in analyzing the dynamics of marine structures and are categorized into first-order wave-frequency (WF) forces and second-order wave drift forces. The total wave-induced forces and moments are expressed as:

$$\boldsymbol{\tau}_{\text{wave}}^{b} = \boldsymbol{\tau}_{\text{wave1}}^{b} + \boldsymbol{\tau}_{\text{wave2}}^{b}. \tag{7}$$

In this study, the force response amplitude operators (RAOs) were used to compute wave-induced forces. They were obtained through frequency-domain potential flow analysis using WAMIT, relate the wave amplitudes to the forces and the moments for a specific craft geometry. The wave loads are calculated by

$$\boldsymbol{\tau}_{\text{wave}}^{b} = \int S(\omega)\cdot \text{RAO}(\omega)\, d\omega. \tag{8}$$

## 5. CASE STUDY

### 5.1 Overview

Table 3. Physical parameters for the unmanned sailboat platform

| Component | Parameter | Value | Unit | Installation position in $\{b\}$ [m] |
|---|---|---|---|---|
| **Hull** | Length overall ($LoA$) | 3.2 | m | |
| | Beam ($B$) | 0.7 | m | |
| | Draft with keel ($D$) | 1.0 | m | |
| **Foils** | Sail area ($A_s$) | 1.5 | $\text{m}^2$ | $[0.4,\ 0,\ -0.4]^\top$ |
| | Rudder area ($A_r$) | 0.15 | $\text{m}^2$ | $[-1.5,\ 0,\ 0]^\top$ |
| | Keel area ($A_k$) | 0.16 | $\text{m}^2$ | $[0,\ 0,\ 0.1]^\top$ |

To evaluate the physical consistency and fidelity of the proposed model, numerical simulations are implemented

in MATLAB/Simulink. The set of physical parameters for the unmanned sailboat platform is provided in Table 3. The validation focused on two key aspects: the sail/rudder force characterization under varying angles, and the hull dynamic response to wave-induced excitations.

### 5.2 Sail and rudder dynamics

A series of static force tests were performed to characterize the aerodynamic and hydrodynamic forces generated by the sail and rudder. The tests were carried out by exposing the sail and rudder to uniform external flow fields, simulating either wind or water current. The environmental conditions were specified as a uniform wind field with a speed of 10 m/s and a steady ocean current of 1 m/s, both oriented along the negative $x$-axis (i.e., direction $\pi$ in the inertial frame $\{n\}$). The sail angle was varied from 0° to 90°, and the rudder angle from 0° to 45°, covering a representative range of operational deflections.

For Reynolds numbers Re $\in [10^4, 10^7]$, the lift and drag coefficients for the NACA 0012 airfoil, adopted for the sail, rudder, and keel profiles in this study, are approximated based on the data provided in (Sheldahl and Klimas, 1981). The CoE is located at the quarter-chord point (Collinson, 2003), consistent with conventional aerodynamic assumptions. In the modeled angle of attack range $\alpha \in [-180°, 180°]$, the lift coefficient $C_L$ varies approximately from -1.2 to 1.2, while the drag coefficient $C_D$ spans from 0.01 to 1.8.

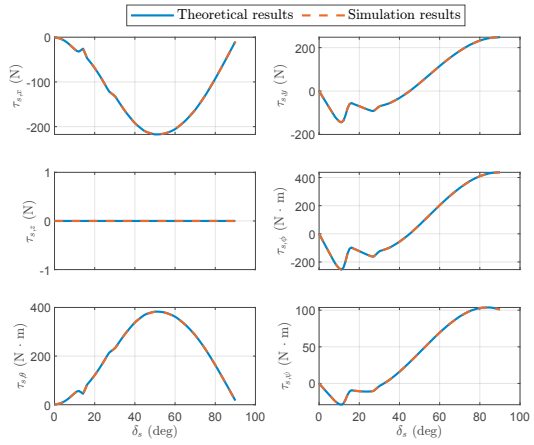


Fig. 3. Simulated and theoretical sail forces and moments under varying sail angles.

The 6-DoF aerodynamic and hydrodynamic forces and moments were recorded across the full range of sail and rudder angles. The simulation results were compared with the theoretical predictions computed from the above lift and drag coefficients. In the theoretical sail or rudder model, the resulting forces and moments are assumed to act at a single CoE, providing a lumped approximation of the distributed foil loads. As shown in Figs. 3–4, the simulated results show close agreement with the theoretical values, confirming the validity and accuracy of the discretized panel-based force modeling method.

### 5.3 Hull hydrodynamics

The hull response was analyzed under irregular wave conditions through three distinct test cases i.e., Case 1:

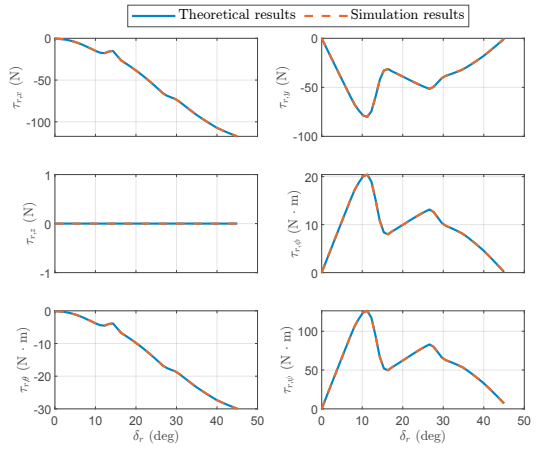


Fig. 4. Simulated and theoretical rudder forces and moments under varying rudder angles.

First-order WF forces only. Case 2: Second-order wave drift forces only. Case 3: Combined 1st- and 2nd-order wave-induced excitations.

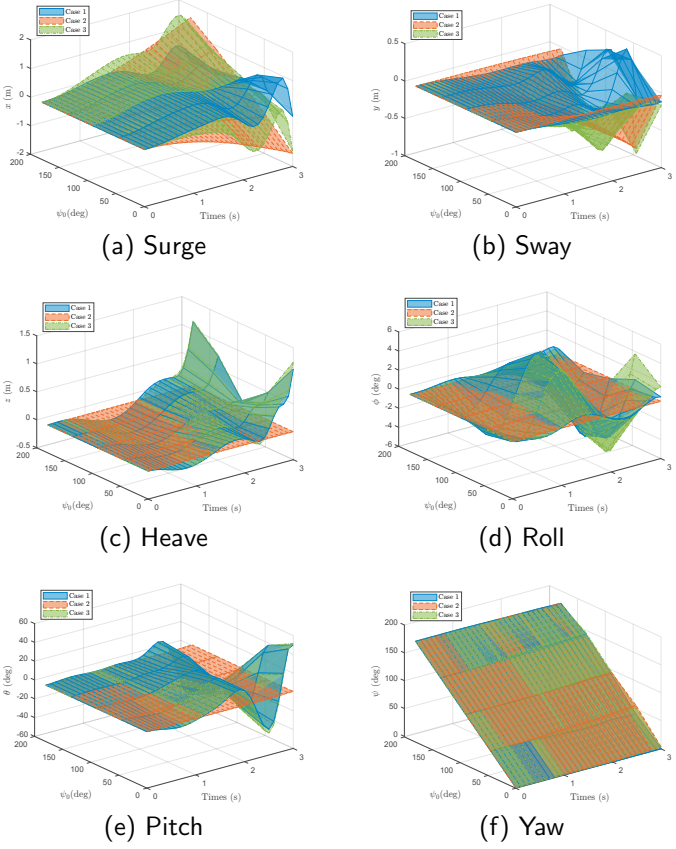


Fig. 5. Simulated 6-DoF hull motion responses under first-order, second-order, and combined wave-induced excitations.

The significant wave height $H_s$ is set to 0.5 m, and the peak period $T_p$ (this is equivalent to the modal period, $T_0$) is chosen as 2.5 s, representing a moderate sea state. The peakedness factor $\gamma$ is selected as 3.3 (Hasselmann, 1973).

Simulated time-domain responses in 6-DoF under each wave loading condition are illustrated in Fig. 5. The results

demonstrate the model's ability to distinguish between oscillatory and slowly varying motion components, and to capture the dynamic effects of both first- and second-order hydrodynamic forces, thereby further validating the model's physical consistency and fidelity.

## 6. CONCLUSION

This study presents a high-fidelity process plant model for unmanned sailboats, integrating 6-DoF multi-body dynamics with the aerodynamic and hydrodynamic forces under realistic wind and wave conditions. The model captures the tightly coupled dynamics of the sail, rudder, keel, and hull, incorporating precomputed CFD-based lift and drag coefficients and frequency-domain hydrodynamic responses from WAMIT. The use of a Morison equation-based approach, combined with the foil discretization and discrete summation over panels, enables accurate computation of forces acting on all foil elements. The model's physical consistency and fidelity are demonstrated through static force testing and dynamic response validation under wave-induced excitations. Future work will focus on the dynamic wave load modeling and intelligent control strategies.

## REFERENCES


An, Y., Yu, J., and Zhang, J. (2021). Autonomous sailboat design: A review from the performance perspective. *Ocean Engineering*, 238, 109753.

Chen, Y., Ding, Y., Hu, Z.Z., and Ren, Z. (2025). Geometrized task scheduling and adaptive resource allocation for large-scale edge computing in smart cities. *IEEE Internet of Things Journal*.

Collinson, R. (2003). *Introduction to Avionics Systems*. Springer.

Deng, Y., Zhang, X., and Zhang, G. (2019). Line-of-sight-based guidance and adaptive neural path-following control for sailboats. *IEEE Journal of Oceanic Engineering*, 45(4), 1177–1189.

Fossen, T.I. (2011). *Handbook of Marine Craft Hydrodynamics and Motion Control*. John Wiley & Sons Ltd.

Gu, N., Wang, D., Peng, Z., Wang, J., and Han, Q.L. (2022). Disturbance observers and extended state observers for marine vehicles: A survey. *Control Engineering Practice*, 123, 105158.

Hasselmann, K. (1973). Measurements of wind-wave growth and swell decay during the joint north sea wave project (jonswap). *Dtsch.Hydrogr.Z*, 8.

Ma, C., Zhang, T., Jiang, Z., and Ren, Z. (2025). Dynamic analysis of lowering operations during floating offshore wind turbine assembly mating. *Renewable Energy*, 122528.

Peng, B., Gu, N., Wang, D., Li, T., Han, B., and Peng, Z. (2023). Online learning-based active disturbance rejection control of autonomous surface vehicles with HIL simulations. *Ocean Engineering*, 288, 116041.

Peng, B., Gu, N., Wang, D., and Peng, Z. (2022). Model-free adaptive disturbance rejection control of an rsv with hardware-in-the-loop experiments. *IEEE Transactions on Industrial Electronics*, 70(7), 7507–7510.

Peng, B., Gu, N., Wang, D., and Peng, Z. (2025). Finite-time parameter self-learning disturbance rejection control of msv: Methodology and validation. *IEEE/CAA Journal of Automatica Sinica*.

Peng, Z., Wang, J., Wang, D., and Han, Q.L. (2021). An overview of recent advances in coordinated control of multiple autonomous surface vehicles. *IEEE Transactions on Industrial Informatics*, 17(2), 732–745.

Plumet, F., Petres, C., Romero-Ramirez, M.A., Gas, B., and Ieng, S.H. (2014). Toward an autonomous sailing boat. *IEEE Journal of Oceanic Engineering*, 40(2), 397–407.

Qin, H., Xu, P., Zhang, F., and Xue, Y. (2024). An improved los guidance and sail-rudder cooperative controller for the path tracking of unmanned sailboats. *IEEE Transactions on Intelligent Vehicles*.

Qin, M., Shi, W., Chai, W., Fu, X., Li, L., and Li, X. (2023). Extreme structural response prediction and fatigue damage evaluation for large-scale monopile offshore wind turbines subject to typhoon conditions. *Renewable energy*, 208, 450–464.

Ren, Z., Jiang, Z., Skjetne, R., and Gao, Z. (2018). Development and application of a simulator for offshore wind turbine blades installation. *Ocean Engineering*, 166, 380–395.

Shah, K.A., Meng, F., Li, Y., Nagamune, R., Zhou, Y., Ren, Z., and Jiang, Z. (2021). A synthesis of feasible control methods for floating offshore wind turbine system dynamics. *Renewable and Sustainable Energy Reviews*, 151, 111525.

Sheldahl, R.E. and Klimas, P.C. (1981). Aerodynamic characteristics of seven symmetrical airfoil sections through 180-degree angle of attack for use in aerodynamic analysis of vertical axis wind turbines. Technical report, Sandia National Lab. (SNL-NM), Albuquerque, NM (United States).

Sun, Q., Qi, W., Liu, H., Sun, Z., Lam, T.L., and Qian, H. (2020). Oceanvoy: A hybrid energy planning system for autonomous sailboat. In *2020 IEEE/RSJ International Conference on Intelligent Robots and Systems (IROS)*, 2481–2487. IEEE.

Tipsuwan, Y., Sanposh, P., and Techajaroonjit, N. (2023). Overview and control strategies of autonomous sailboats—a survey. *Ocean Engineering*, 281, 114879.

Viel, C., Vautier, U., Wan, J., and Jaulin, L. (2019). Platooning control for heterogeneous sailboats based on constant time headway. *IEEE Transactions on Intelligent Transportation Systems*, 21(5), 2078–2089.

Wang, S., Xing, Y., Balakrishna, R., Shi, W., and Xu, X. (2023). Design, local structural stress, and global dynamic response analysis of a steel semi-submersible hull for a 10-mw floating wind turbine. *Engineering Structures*, 291, 116474.

Xiao, L. and Jouffroy, J. (2013). Modeling and nonlinear heading control of sailing yachts. *IEEE Journal of Oceanic Engineering*, 39(2), 256–268.

Zhang, G., Li, J., Jin, X., and Liu, C. (2021). Robust adaptive neural control for wing-sail-assisted vehicle via the multiport event-triggered approach. *IEEE Transactions on Cybernetics*, 52(12), 12916–12928.

Zhang, T. and Ren, Z. (2025). Restricted isometry property in wave buoy analogy and application to multispectral fusion. *IEEE Transactions on Intelligent Transportation Systems*.